Journal of Materials Chemistry A

PAPER

View Article Online
View Journal | View Issue

Cite this: J. Mater. Chem. A, 2018, 6, 21558

IrOOH nanosheets as acid stable electrocatalysts for the oxygen evolution reaction†

Daniel Weber, ‡[ab] Leslie M. Schoop,[c] Daniel Wurmbrand,[d] Sourav Laha,[a] Filip Podjaski,[ae] Viola Duppel,[a] Kathrin Müller,[a] Ulrich Starke[a] and Bettina V. Lotsch *[abf]

Received 15th August 2018
Accepted 5th October 2018

DOI: 10.1039/c8ta07950a

rsc.li/materials-a

In solids, heterogeneous catalysis is inherently bound to reactions on the surface. Yet, atomically efficient preparation of specific surfaces and the characterization of their properties are impeding its applications towards a clean energy future. Here, we present the synthesis of single layered IrOOH nanosheets and investigations of their structure as well as their electrochemical properties towards oxygen evolution under aqueous acidic conditions. The nanosheets are synthesized by treating bulk IrOOH with a tetrabutylammonium hydroxide solution and subsequent washing. Electron diffraction shows that the triangular arrangement of the edge sharing $Ir(O,OH)_6$ octahedra found in the layers of bulk IrOOH is retained after exfoliation into single layers. When incorporated as an active component in Ti electrodes, the nanosheets exhibit a Tafel slope of 58(3) mV dec^{-1} and an overpotential of $\eta_{10\ mA\ cm^{-2}} = 344(7)$ mV in 0.1 M $HClO_4$, while retaining the trivalent oxidation state of iridium. They outperform bulk rutile-IrO_2 and bulk IrOOH as electrocatalytic water oxidation catalysts under the same conditions. The results of this study on the structure–property relationships of low valence IrOOH nanosheets offer new pathways for the development of atom efficient, robust and highly active oxygen evolution catalysts.

1 Introduction

Electrochemical splitting of water into hydrogen and oxygen is of immense technological interest to realize hydrogen as a storage medium for the energy generated from renewable resources.[1] Even though the generation of hydrogen is the main goal, the oxygen evolution reaction (OER) is the bottleneck in this process.[2,3] Due to the number of complex intermediates and the need to transfer four electrons instead of two in a concerted fashion, this reaction is kinetically challenging, leading to a higher overpotential needed to drive the oxidation of water. Apart from these energetic requirements, OER catalysts also have to be cheap to manufacture, stable over time and chemically resistant to environments of high and/or low pH values.[4]

While many newly investigated catalysts meet most of these stringent requirements,[5–10] none of them can compete with ruthenium oxide and iridium oxide regarding catalysis in acidic media. Rutile-type IrO_2 (rutile-IrO_2) is a state-of-the-art catalyst and it is used to benchmark the activities of new materials due to its high stability against decomposition under acidic conditions.[11]

To keep iridium oxide catalysts competitive despite their very low natural abundance, strategies such as nanostructuring, scaffolding and electronic design have been applied to increase their OER activity whilst minimizing the amount of active catalyst material. The synthesis of nanoparticles shows great promise, as a small overpotential of $\eta = 0.25$ V generates a current density of 4 μA cm_{ox}^{-2} in rutile-IrO_2 nanoparticles with a diameter of 7 nm.[12] Yet, at this diameter, the nanoparticles consist of only a few unit cells, leaving little space for further size reduction. While other nanostructures such as nanorods,[13] thin films[14] and mesoporous IrO_2 (ref. 15) were explored, none of them have yielded atomically thin catalysts. Other highly relevant investigations are focused on IrO_x, an amorphous catalyst containing mixed valence iridium octahedrally coordinated by oxide, hydroxide and water ligands.[16–19] The presence of trivalent iridium and the high surface area of the amorphous state are both prerequisites for excellent OER activity, which surpasses that of rutile-IrO_2.

In two more recent papers, the promising electrocatalytic properties of IrO_2 nanosheets have been explored.[20,21] The

[a]Max Planck Institute for Solid State Research, Heisenbergstrasse 1, 70569 Stuttgart, Germany. E-mail: b.lotsch@fkf.mpg.de
[b]Ludwig-Maximilians-Universität München, Butenandtstrasse 5-13, 81377 Munich, Germany
[c]Princeton University, Princeton, USA
[d]University of Konstanz, Konstanz, Germany
[e]Ecole Polytechnique Fédérale de Lausanne, Station 12, 1015 Lausanne, Switzerland
[f]Nanosystems Initiative Munich (NIM) and Center for Nanoscience (CeNS), Schellingstrasse 4, 80799 Munich, Germany

† Electronic supplementary information (ESI) available: Additional details on experimental procedures, SEM images of the electrodes and electrochemical data on iridium oxide based catalysts. See DOI: 10.1039/c8ta07950a

‡ Present address: Ohio State University, Columbus OH, USA.

investigated material is layered and crystalline and acts as a catalyst towards OER in 0.1 M $HClO_4$ with a Tafel slope of 57–62 mV dec^{-1}. Due to the lack of other electrochemical parameters, *e.g.* the overpotential, as well as the crystal structure of the material, no structure–property–activity relationships were established.

Here, we present IrOOH nanosheets prepared from recently investigated bulk IrOOH *via* the tetrabutylammonium hydroxide (TBAOH) exfoliation route. The results of our investigation link the structure of the nanosheets and their electrochemical behavior. We studied this system due to the layered nature of the parent compound as well as the rare oxidation state of Ir observed in the bulk material.[22] Similar to the bulk compound, the nanosheets consist of a triangular arrangement of $Ir^{III}(O,OH)_6$ octahedra and are stable in acidic environments. Yet, due to an advantageous combination of single layer morphology and a low iridium valence state, the IrOOH nanosheets surpass both bulk IrOOH and rutile-IrO_2 as catalysts for the OER under the same conditions.

2 Results and discussion

2.1 Preparation and structure of IrOOH nanosheets

IrOOH nanosheets were prepared by an ultrasonication-assisted exfoliation of bulk IrOOH (obtained by acid treatment of $K_{0.75}Na_{0.25}IrO_2$) in an aqueous TBAOH solution and subsequent washing. The resulting dispersion was deep blue as displayed in the inset in Fig. 1a, similar to the bulk IrOOH powder. The nanosheets were stabilized by a zeta-potential of −36.4 mV, indicating a negatively charged surface as well as an intermediate dispersion stability *versus* agglomeration. Dispersions of the monolayers were stable against agglomeration for 4–6 weeks.

The IrOOH nanosheets could easily be deposited on various surfaces, either on SiO_2–Si substrates (270 nm SiO_2, thermally grown) as displayed in Fig. 1 or on Ti substrates (Fig. S3†). After drying, no redispersion of the deposited layers was observed upon wetting with water, which indicates the absence of TBA^+ and its hydrate shell. The single layers have lateral dimensions between 0.5 and 7 μm and are 1.02(8) nm in height, as can be seen in Fig. 1b. The monolayer height differs from the height of 0.5 nm of a single crystalline slab in the bulk[22] due to a layer of water surrounding the nanosheet, which is subsequently trapped between the nanosheet and the underlying support.[23]

Before washing, a nanosheet layer height of 1.60(8) nm was observed, which suggests the presence of TBA^+ between the nanosheet and the substrate. Upon washing, TBA^+ is removed and the height reduced from 1.6 to 1.0 nm. The difference coincides with the height of the TBA^+ cation. The absence of TBA^+ is also indicated by the energy dispersive X-ray spectroscopy (EDX) line scans in transmission electron microscopy (TEM), where no nitrogen was detected.

The in-plane structure of the IrOOH nanosheets was investigated by TEM with selected area electron diffraction (SAED), EDX on single nanosheets and powder X-ray diffraction (PXRD) on a nanosheet pellet. Fig. 2a depicts an exemplary TEM bright field image of several translucent IrOOH nanosheets.[22] The

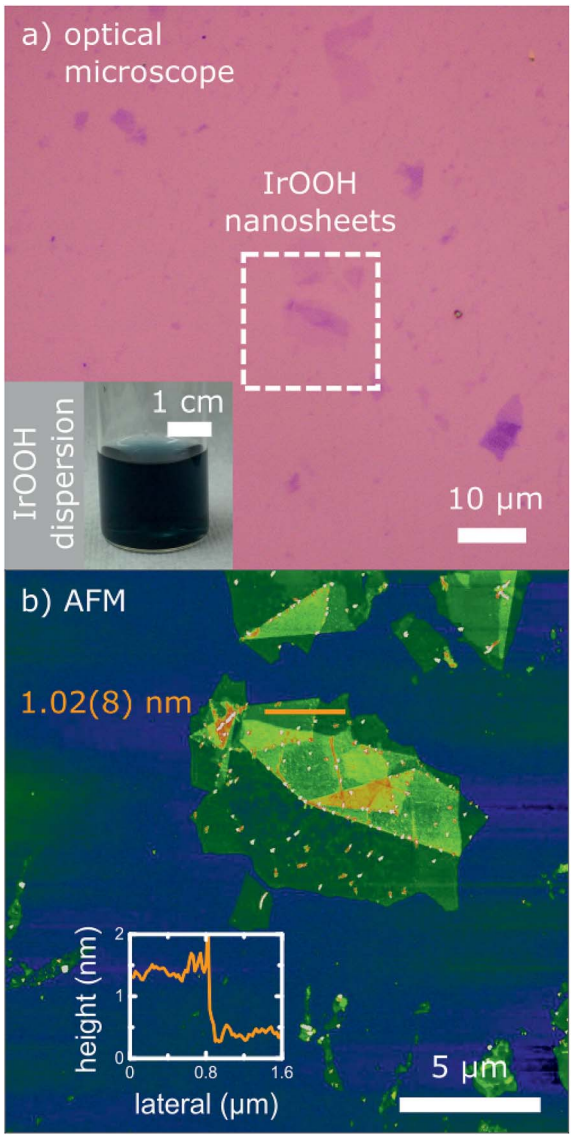

Fig. 1 (a) Optical microscope and (b) AFM image of the IrOOH nanosheets; the inset of (a) shows the dark blue aqueous dispersion of the nanosheets; inset of (b) displays an exemplary height profile with an average height value of a single layer of IrOOH measured on a SiO_2 (270 nm)–Si substrate.

translucency towards the electron beam is typical for very thin samples and indicates that the specimen consists of one or a few layers. TEM-EDX measurements showed that the ratio of iridium to oxygen was Ir : O = 1 : 2.3 measured on the Ir M-line and O K-line. Considering the high uncertainty in the detection of light elements such as oxygen using the EDX detectors, this ratio is close to the ideal stoichiometry of Ir : O for IrOOH. No nitrogen was detected, indicating the absence of TBA^+. We therefore assume that charge neutrality is attained by protonation of the $[IrO_2]^-$ backbone. SAED revealed a hexagonal diffraction pattern, which was compared to a simulation based on the crystallographic data of bulk IrOOH as depicted in Fig. 2b and c. The reflections were indexed based on the bulk

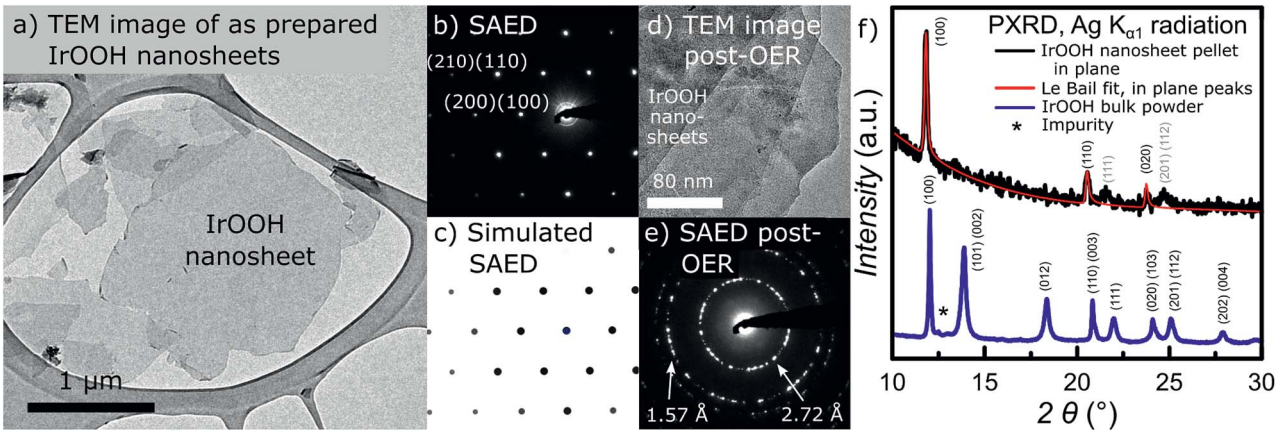

Fig. 2 (a) TEM image and (b) SAED pattern of the IrOOH nanosheets, (c) simulated SAED pattern based on the crystallographic data from bulk IrOOH in the space group $P\bar{3}m1$ along [001] zone axis; (d) TEM image and (e) SAED pattern of the IrOOH nanosheets after electrocatalysis; (f) PXRD pattern of the IrOOH nanosheet pellet; the small and broad peaks at $2\theta = 22°$ and 25° probably arise from the (111), (201) and (112) reflections, indicating some degree of order along the *c*-direction in the restacked nanosheet pellet.

IrOOH structure with the *d*-values $d_{(100)} = 2.71$ Å, $d_{(110)} = 1.56$ Å, $d_{(020)} = 1.35$ Å, $d_{(210)} = 1.02$ Å and $d_{(030)} = 0.90$ Å.[22]

In order to verify the structural integrity of the IrOOH nanosheets under anodic conditions, we analyzed a multilayer nanosheet film by TEM imaging and SAED after electrocatalysis, which resulted in the image and diffraction pattern displayed in Fig. 2d and e. The IrOOH nanosheet film catalyzed the OER under chronopotentiometric conditions at $j = 1$ mA cm^{-2} in 0.1 M $HClO_4$ for 7 h and was mechanically removed from the Ti substrate prior to analysis. The TEM image of the post OER-catalysis IrOOH nanosheet film reveals a multilayer consisting of several nanosheets, similar to the nanosheet film prior to catalysis as shown in Fig. S3.† The SAED pattern shows rings of reflections typical for multilayers of nanosheets which form during the creation of the electrodes on the Ti substrate. The observed *d*-values of $d_{(100)} = 2.72$ Å and $d_{(110)} = 1.57$ Å indicate the retention of the in-plane crystal structure after catalysis. Thus, the retention of the nanosheet morphology as well as the crystal structure highlights the extraordinary chemical stability of IrOOH under anodic conditions.

PXRD on a pellet of the nanosheet in transmission geometry yields the in-plane diffraction patterns shown in Fig. 2f. The structural model with the lattice parameters $a = 3.136$ Å and $c = 91.61$ Å was fitted to the diffraction patterns using the LeBail method. The turbostratic disorder introduced by restacking was simulated by the expanded *c*-lattice parameter.[24,25] The reflections with the main intensity were indexed based on the structure of bulk IrOOH and were identified as $d_{(100)} = 2.72$ Å, $d_{(110)} = 1.57$ Å, and $d_{(020)} = 1.36$ Å. The small, broad reflections at $2\theta = 22°$ and 25° indicate the introduction of some degree of order during the restacking of the nanosheets.

A comparison of the diffraction data of the nanosheets and known layered bulk compounds is listed in Table 1. The results from the SAED measurements of the nanosheets only slightly deviate from the values obtained from TEM and X-ray diffraction of the bulk compounds. As the deviations are well within the margin of error of electron diffraction (≈5%) and TEM-EDX suggests a composition close to the formula IrO_2, the data indicate the retention of the in-plane structure and composition of IrOOH during the exfoliation process. The results were reproducible for single nanosheets (TEM) as well as an ensemble of nanosheets in the form of a pellet (PXRD). Consequently, the nanosheets dispersed in water consist of a triangular layer of the edge sharing IrO_6 octahedra, similar to the nanosheets of $[MnO_2]^{x-}$, $[CoO_2]^{x-}$, and $[RuO_2]^{x-}$,[26–28] as well as the structure of a slab of brucite-type $Mg(OH)_2$.

The IrOOH nanosheets are structurally and chemically related to other systems which are relevant to electrocatalysis, as displayed in Fig. 3. The first related material is an electrocatalytically activated Ir–Ni mixed oxide thin film system, which features SAED patterns similar to a layered brucite-type structure with increasing Ni content while being X-ray amorphous.[29] Under highly corrosive anodic conditions, Ni is leached out, leaving behind a porous surface with an extraordinarily high

Table 1 Comparison of *d*-values from TEM of an IrOOH single layer, TEM of bulk IrOOH, PXRD and single crystal X-ray diffraction (SXRD) of $K_{0.75}Na_{0.25}IrO_2$

(*hkl*)	IrOOH nanosheet TEM, *d* [nm]	IrOOH nanosheet PXRD, *d* [nm]	IrOOH bulk TEM, *d* [nm]	IrOOH bulk PXRD, *d* [nm]	$K_{0.75}Na_{0.25}IrO_2$ bulk SXRD, *d* [nm]
(100)	0.267	0.272	0.271	0.270	0.272
(110)	0.154	0.157	0.156	0.156	0.157
(020)	0.134	0.136	0.135	0.135	0.136
(210)	0.101		0.102	0.102	0.103
(030)	0.089		0.090	0.090	0.091

hydroxyl surface coverage, as displayed schematically in Fig. 3b and discussed in more detail further below. Other related compounds include the highly active oxyhydroxides of the 3d transition metals Mn, Fe, Co, and Ni as well as the layered double hydroxides.[9,30] The structure of a CoOOH layer is shown in Fig. 3c. The oxyhydroxide electrocatalysts exhibit some of the lowest overpotentials with regard to OER catalysis for medium to high pH values. Further enhancement in the activity of these layered catalysts was achieved by exfoliation, doping, or the addition of phosphate or borate buffers.[9,31,32] The IrOOH nanosheets also structurally resemble the (2×2) iridium oxide overlayer, which grows on the Ir(111) surface under low oxygen pressures at room temperature.[33] The structure model that best describes the measured data is displayed in Fig. 3d, where the oxygen atoms reside above or below the vacancy in the triangular top layer of iridium. An Ir–O distance of 2.04 Å has been observed, a value similar to the Ir–O distances of 2.070(5) Å and 2.041(4) Å in $K_{0.75}Na_{0.25}IrO_2$ and bulk IrOOH, respectively, obtained from X-ray diffraction.[22]

Recent work reported on the nanosheets of IrO_2[20] which could have a structure similar to the IrOOH nanosheets presented here. The similar in-plane lattice parameters of 3.1 Å as well as the presence of trigonal/hexagonal symmetry within the plane hint at similarities between the nanosheets of IrO_2 and the IrOOH nanosheets prepared by our method. In the following paragraph, we present the relation between the crystal structure and electrochemical properties of the IrOOH nanosheets.

2.2 Electrochemical characterization

To investigate the relationship of the IrOOH structure and its electrochemical properties, the IrOOH nanosheets were incorporated into electrodes by drop-casting the nanosheet dispersion onto titanium. Our deposition approach utilizes the intermediate stability of the IrOOH nanosheet dispersion and the subsequent agglomeration upon evaporation of the solvent. Electrodes were prepared by heating Ti platelets in an aqueous solution of oxalic acid to remove the surface oxide and then drop-casting an ink of the catalyst onto the Ti substrate heated to 160 °C, followed by annealing for 30 min at the same temperature to remove the residual solvent.[34] Once the sheets agglomerate on the Ti surface, they do not redisperse, thus eliminating the need for a binder. This is crucial, as possible carbon-based binders have limited stability at the high potentials required during electrolysis in acidic media.[35] At least five as-prepared dimensionally stable anodes (DSA) with loadings of 0.2 mg cm^{-2} and a geometric surface area of 1 cm^2 were characterized for the IrOOH nanosheets, bulk IrOOH and rutile-IrO_2 in a water splitting setup with an Ag/AgCl/saturated KCl reference electrode, which is schematically depicted in Fig. 4a. The nanosheet coverage of the Ti substrate was estimated to be greater than 95% of the substrate surface from SEM, as only very few spots of the bare Ti substrate were found by back scattered electron detection. The SEM images and additional comments on the electrode coverage are presented in the ESI.† The electrocatalytic properties of the IrOOH nanosheets were investigated by collecting the current–voltage curves of a 0.1 M $HClO_4$ electrolyte. The activities were compared to those of bulk IrOOH and bulk rutile-IrO_2 in terms of the Tafel slope, overpotential at 10 mA cm^{-2} and the current density at 300 mV of overpotential. The current–voltage data were fitted to the Tafel equation (eqn (1)),

$$\eta = b \log \frac{j}{j_0} \quad (1)$$

where η is the overpotential, b is the Tafel slope, j is the current density, and j_0 is the exchange current density. The data were corrected by subtracting the open circuit potential of a hydrogen saturated Pt/Pt electrode couple and applying a correction for the internal resistance, thereby excluding the effect of variations of the pH. The Tafel slope was determined from individual fits of five different samples of the same material. The error results from the standard deviation of the average value. The stability of the electrodes was tested by chronopotentiometry at 1 and 10 mA cm^{-2}. The plots of the collected data are displayed in Fig. 4b and c.

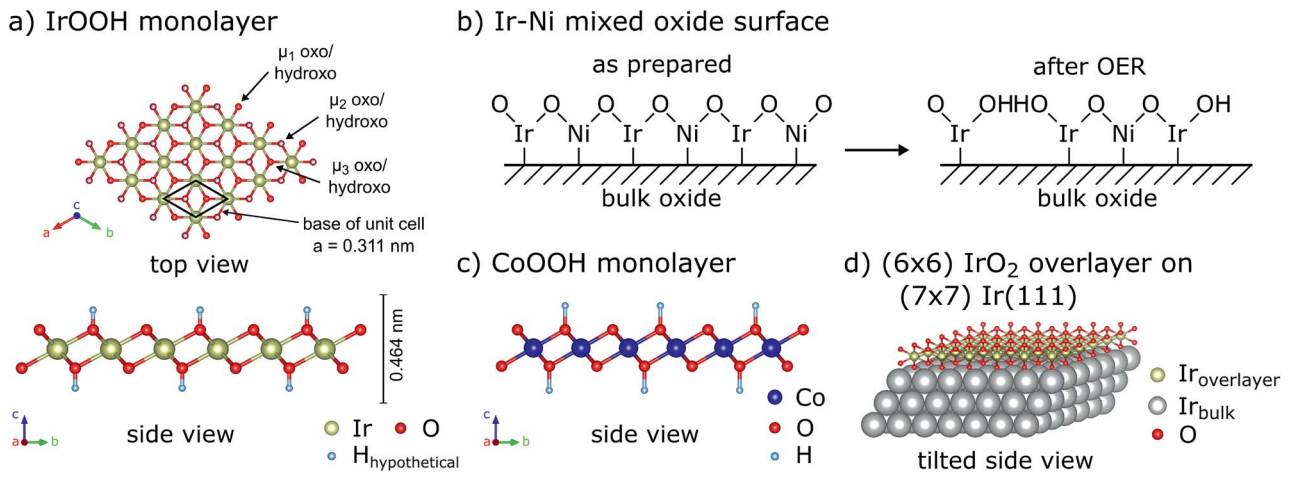

Fig. 3 (a) Top and side views of the IrOOH nanosheet structure, μ-oxo/hydroxo-bridges indicated, (b) schematic of acid leaching in Ir–Ni mixed oxide according to Reier *et al.*,[29] (c) side view of a CoOOH monolayer[9,30] and (d) tilted side view of the (2×2) IrO_2 overlayer on Ir(111).[33]

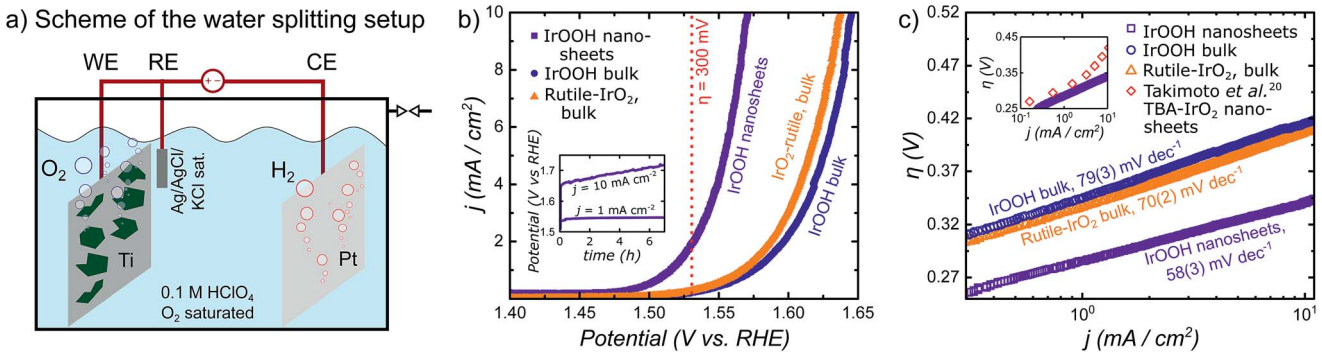

Fig. 4 (a) Scheme of the water splitting setup; (b) plot of the current density j *vs.* the potential with a visual cue for the readout of j at $\eta = 0.3$ V; the inset shows chronopotentiometry at $j = 1$ and 10 mA cm^{-2}; (c) Tafel plot of the overpotential η *vs.* the logarithmic representation of the current density j and the extracted Tafel slopes; the inset of (c) shows comparison of the IrOOH nanosheets and IrO_2 nanosheets reported by Takimoto *et al.*[20]

The Tafel slope was extracted by fitting the Tafel equation to the linear region of the plot of η *vs.* $\log j$. We found bulk rutile-IrO_2 and IrOOH to have Tafel slopes of 70(2) mV dec^{-1} and 79(3) mV dec^{-1}, respectively, while electrodes modified with IrOOH nanosheets feature a slope of 58(3) mV dec^{-1}. Previously, a Tafel slope of approximately 60 mV dec^{-1} has been found in the bulk rutile-IrO_2 electrocatalysts investigated under acidic conditions. A Tafel slope of this magnitude has been associated with the restructuring process between two energetically inequivalent surface bound hydroxyl groups.[36,37] The restructuring of these hydroxyl groups might also be responsible for the rate determining step in bulk IrOOH and nanosheets; however, more careful systematic investigations are needed to elucidate the surface chemistry of IrOOH. As seen in the inset of Fig. 4c, the nanosheets of IrOOH and IrO_2 (ref. 20) show similarities in the Tafel slope, thus indicating that the previously reported IrO_2-nanosheets feature a similar catalytically active environment.

The overpotential η needed to drive the OER was calculated for a current density of $j = 10$ mA cm^{-2} utilizing the Tafel equation. The current density of $j = 10$ mA cm^{-2} mimics the output of a high end solar to hydrogen device with 12% efficiency.[9] The overpotentials of bulk rutile-IrO_2 and IrOOH are $\eta_{10\ \mathrm{mA\ cm^{-2}}} = 415(5)$ mV and $\eta_{10\ \mathrm{mA\ cm^{-2}}} = 433(5)$ mV, respectively. The IrOOH nanosheets exhibit a significantly reduced overpotential of $\eta_{10\ \mathrm{mA\ cm^{-2}}} = 344(7)$ mV. After a small initial increase, the OER potential of the nanosheet electrodes remained constant for $j = 1$ mA cm^{-2} over 7 h, as seen in the inset of Fig. 4b. As chronopotentiometry was performed in 0.1 M $HClO_4$, the measurements prove the acid stability of the IrOOH nanosheet electrodes. At a current density of 10 mA cm^{-2}, the intense O_2 gas bubble formation led to a ragged chronopotentiometric curve as well as to visually observable catalyst ablation and thus a gradual reduction in activity.

A third descriptor used to compare the performance of the electrocatalysts is the current density j measured at an overpotential of 300 mV. Bulk rutile-IrO_2 and IrOOH have relatively low current densities of $j_{300\ \mathrm{mV}} = 0.217(7)$ mA cm^{-2} and $j_{300\ \mathrm{mV}} = 0.172(15)$ mA cm^{-2}, respectively, while the current density of the nanosheet electrodes at $\eta = 300$ mV is approximately one order of magnitude larger with $j_{300\ \mathrm{mV}} = 1.8(4)$ mA cm^{-2}. The high current density observed in the nanosheet electrodes could potentially indicate a higher reaction rate of the nanosheets compared to that of the bulk materials. Thus, exfoliation results in an increased electrocatalytic activity of the nanosheets compared to the bulk compounds, as described by the summary of the three electrocatalytic indicators in Table 2.

2.3 X-ray photoelectron spectroscopy

To verify the retention of the trivalent oxidation state specific to the IrOOH nanosheets, the nanosheet electrodes were characterized by X-ray photoelectron spectroscopy (XPS) after electrolysis and compared to bulk IrOOH and bulk rutile-IrO_2. The Ir $4f_{7/2}$ and $4f_{5/2}$ peaks observed in each spectrum were fitted with two components and additional satellites according to the Wertheim–Kotani model, which states that more than one component is necessary for the fit due to the asymmetric peak shape.[38] The peak shapes become less asymmetric when going from rutile-IrO_2 to bulk and nanostructured IrOOH, which has been associated with a decrease in metallicity.[29] The iridium valence state was analyzed by comparing the position of the Ir $4f_{7/2}$ and $4f_{5/2}$ peaks, which were observed at 62.3 eV and 65.33 eV in the spectra of the nanosheet electrodes after 60 cycles of cyclic voltammetry at 5 mV s^{-1} between 1.0 V and 1.5 V (*vs.* Ag/AgCl). Bulk IrOOH and bulk rutile-IrO_2 featured peaks at 62.5 and 65.5 eV as well as 61.8 and 64.8 eV, respectively, with the related spectra and fits depicted in Fig. 5. The 4f iridium binding energies in the nanosheet electrode samples are in almost perfect agreement with the binding energies of bulk

Table 2 Comparison of b, η and j of the IrOOH nanosheets, bulk IrOOH and rutile-IrO_2

Active electrode material	Tafel slope b [mV dec^{-1}]	η at 10 mA cm^{-2} [mV]	j at 300 mV [mA cm^{-2}]
IrOOH nanosheets	58(3)	344(7)	1.8(4)
IrOOH bulk	79(3)	433(5)	0.172(15)
Rutile-IrO_2 bulk	70(2)	415(5)	0.217(7)

IrOOH, indicating that iridium is present as a trivalent species surrounded by oxide/hydroxide ions in the IrOOH nanosheets. Similar XPS results on trivalent iridium with an octahedral oxide/hydroxide coordination have been recently reported for crystalline bulk IrOOH,[22] the amorphous OER catalyst IrO_x and a predicted trivalent Ir-defect site in rutile-IrO_2.[19]

2.4 Discussion

In light of these findings, the differences in the electrochemical behavior of the IrOOH nanosheets compared to bulk IrOOH and rutile-IrO_2 can be understood by considering the octahedral connectivity, electron configuration of iridium, morphology variations, changes due to the protonation and density of the surface hydroxyl species. In IrOOH, the [IrO_6] octahedra are edge connected to six neighbors, while one octahedron is edge linked to two octahedra and corner connected to another eight octahedra in rutile-IrO_2. This difference in connectivity could have a sizeable influence on the number of possible configurations as well as the energetic landscape of the active site. Additionally, prior research suggests that tetravalent rutile-IrO_2 with its $5d^5$ electron state is a metallic conductor, while layered IrOOH is a semiconductor with a low spin $5d^6$ electron configuration for trivalent iridium.[22] Such a decrease in valency of the metal center has been correlated with an increased OER activity in mixed valence compounds such as amorphous IrO_x[19,39,40] or the pyrochlore $Y_2Ru_2O_{7-\delta}$.[41] In both examples, the presence of trivalent metal centers has been identified as a critical ingredient for excellent catalytic activity. In bulk IrOOH, Ir is purely trivalent, which leads to the presence of a band gap. While this represents a disadvantage in terms of conductivity, IrOOH can be exfoliated into nanosheets. In our work, these nanosheets showed a reduced overpotential compared to the bulk of IrOOH and rutile-IrO_2. Similar reductions in the OER overpotential of nanosheet materials have been observed in previous investigations on semiconducting layered double hydroxides.[9] There, apart from exposing an increased number of active sites, exfoliation leads to a shortened electron path length and, possibly, a more facile percolation from the conducting substrate through the catalyst to the solid–liquid interface,[9,42] and consequently to smaller interfacial resistances. Exfoliation can also free up the path towards metallic edge states on undercoordinated metal cations, which have been linked to the enhanced catalytic activity for the hydrogen evolution reactions in MoS_2 nanosheets.[43–45] Another potentially beneficial factor is good coverage with hydroxyl species on the catalyst surface, which is 50% in IrOOH. In a previous work, this high hydroxyl coverage was created on the surface of thermally grown Ir–Ni mixed oxide films by leaching of Ni under anodic conditions, as shown in Fig. 3b.[29] There, the porous surface features a high density of weakly bound hydroxy groups, which act as the reactive surface intermediates for the OER. A combination of these effects could explain the decrease in overpotential observed upon the exfoliation of IrOOH, which allows its use as a catalyst at low precious metal loadings.

Additionally, the presented catalyst is interesting when considering the OER mechanism and degradation pathways found in rutile-IrO_2 under anodic conditions. Recent literature suggests that the oxidized metallic Ir films and rutile-IrO_2 catalyse O_2 evolution in a two-electron per Iridium reaction going through Ir^V and Ir^{III} intermediates.[35,46] Degradation occurs either by oxidation of pentavalent Ir oxyhydroxide to water soluble hexavalent IrO_4^{2-} on the active site or by dissolution of oligomeric IrO*x* hydrates containing corner sharing, mixed tri- and tetravalent IrO_6 octahedra.[19,35,39,46] In contrast, the IrOOH nanosheets presented in this work feature a lower valence state of Ir in a motif similar to brucite-type structures such as CoOOH. There, cobalt is trivalent and arranged in layers of edge sharing $Co(O,OH)_6$ octahedra in the resting state. Under OER conditions, the oxidation state of Co cycles between Co^{II}, Co^{III} and Co^{IV}.[47,48] Similarly, the change to trivalent iridium as well as the layered structural motif could shift the balance away from the degradation reactions towards the competing O_2 pathway, thus decreasing the likelihood of oxidative decomposition in the nanosheets. Therefore, the IrOOH nanosheets presented in this work are not only of high interest for fundamental studies on electrocatalytic oxygen evolution from water, but also have the potential to excel in industrial applications.

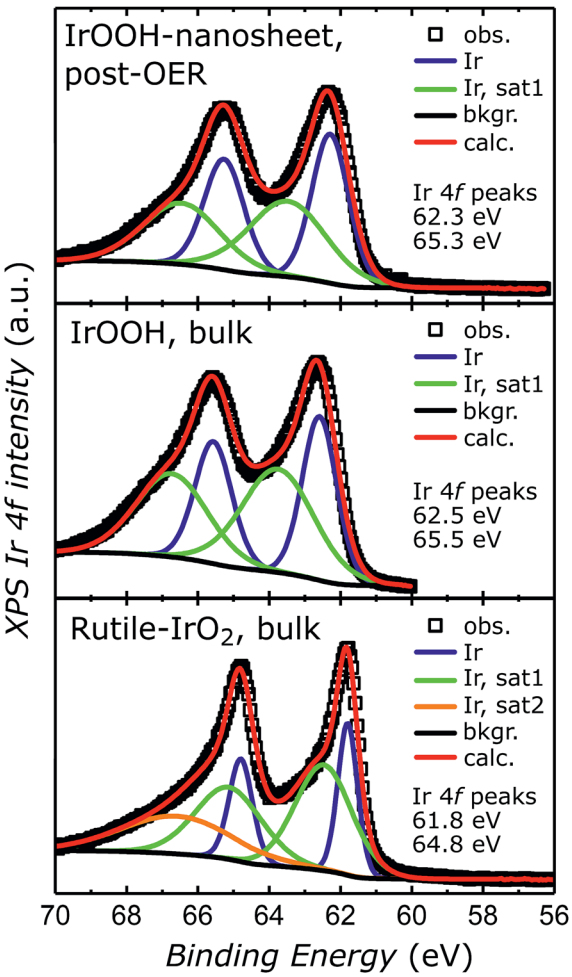

Fig. 5 XPS spectra of the IrOOH nanosheet electrode surface after OER, bulk IrOOH and bulk rutile-IrO_2 in the energy region of the Ir 4f transition.

3 Conclusions

We report a procedure for the exfoliation of bulk IrOOH into an aqueous dispersion of IrOOH nanosheets. TEM images along with SAED patterns show that the single layers retain the triangular lattice of the CdI_2-type structure of the parent compound IrOOH consisting of edge-sharing IrO_6 octahedra. The nanosheets were incorporated into a dimensionally stable anode on titanium and yielded an overpotential of 344 mV at 10 mA cm^{-2} and a Tafel slope of 58 mV dec^{-1}. Thus, exfoliation leads to materials with increased electrocatalytic activity, which is comparative or even superior to that of bulk IrOOH (η = 433 mV, b = 79 mV dec^{-1}) or that of the state-of-the-art catalyst bulk rutile-IrO_2 (η = 415 mV, b = 70 mV dec^{-1}). As chronopotentiometry shows little change in activity and XPS indicates the retention of the trivalent state in iridium after the OER, both methods illuminate the potentially long lifetime of IrOOH nanosheet based catalysts. Thus, the presented material is a promising platform for fundamental studies of low valence iridium as an OER catalyst and could be of great interest for large-scale industrial heterogeneous catalysis.

4 Experimental

4.1 Material preparation

4.1.1 $K_{0.75}Na_{0.25}IrO_2$. The synthesis was adopted from the literature[22] and modified. In a typical experiment, 38.2 mg (0.2 mmol, 1 eq.) of iridium was ground with a flux of 82 mg (0.6 mmol, 3 eq.) 90 wt% K_2CO_3 and 10 wt% Na_2CO_3, and then heated in a corundum crucible in air for 15 h at 900 °C. The product was quenched to room temperature and quickly transferred to an argon filled glove box. The resulting dark grey, powdery mixture was characterized by PXRD; see Fig. S1.†

4.1.2 Bulk IrOOH. The mixture of $K_{0.75}Na_{0.25}IrO_2$ and remaining flux was washed with HCl (1 M, 1 mL mg^{-1}) to exchange the alkali metal ions with protons and to remove the remaining carbonate flux as well as the soluble side phases. The mixture was shaken using an orbital shaker for 5 d; the supernatant acid was decanted and exchanged daily. The final product was washed with water and dried at 100 °C for 30 min. The resulting, violet metallic powder was examined by PXRD.

4.1.3 IrOOH nanosheets. IrOOH (33.8 mg; 1.5 mmol) was soaked in a 10 mM aqueous solution of TBAOH with a molar ratio of TBAOH : IrOOH of 2 : 1. After ultrasonicating the dispersion for 30 min, it was centrifuged at 1000 rpm and the supernatant was separated from the unexfoliated solid components. Subsequently, the supernatant dispersion was centrifuged at 15 000 rpm for 30 min to precipitate the nanosheets, and the TBAOH solution was decanted and exchanged for doubly distilled H_2O, yielding a dark blue dispersion. This exchange of the TBAOH-containing supernatant for water was critical, as the nanosheets deposited from a TBAOH containing solution redispersed after deposition, impeding their electrochemical characterization. To prevent agglomeration, the suspension was stored at 4 °C. The nanosheets were investigated by transmission electron microscopy (TEM) with EDX, atomic force microscopy (AFM), zeta potential and electrochemical measurements. A nanosheet pellet was investigated by transmission powder X-ray diffraction.

4.1.4 Electrode preparation. Ti platelets of dimension 10 mm × 10 mm were ultrasonicated in an aqueous detergent solution, washed with doubly distilled water and subsequently etched in an aqueous solution of 10 wt% oxalic acid for 2 h at a slight boil while stirring.[34] After 60–90 min, the colorless, transparent solution turned brown. The platelets were then washed with water and isopropanol, followed by drying in air. The SEM image of the surface of a neat Ti platelet is displayed in Fig. S2.†

Electrodes of the nanosheets and bulk compound IrOOH and commercially available rutile-IrO_2 were prepared by drop-casting. The nanosheet suspension was drop-cast onto the etched Ti platelets at 160 °C in steps of 0.1 mL until coverage of 0.2 mg cm^{-2} was reached. The substrates were then annealed for 20 min at 160 °C. SEM images of the thus covered Ti platelets are displayed in Fig. S3.† The electrodes of bulk IrOOH and commercially available powder of bulk rutile-IrO_2 were processed into inks by dispersing 4 mg mL^{-1} in an isopropanol water solution (2 : 1, v/v) in an ultrasonic bath for 30 min, then deposited onto the Ti platelets at T = 160 °C and heated for another 20 min. The loaded substrates were contacted to a wire using silver paste and the back side insulated with epoxy glue, yielding electrodes of a 1.00 cm^2 geometrical surface area.

4.2 Characterization

4.2.1 Electrochemical characterization. The electrochemical characterization was conducted as closely as possible to previously reported best practice procedures.[11,49] The prepared electrodes were investigated in a three-electrode setup with 0.1 M $HClO_4$ as the electrolyte. The setup consisted of the working electrode (WE), a platinum counter electrode (CE) as well as a Ag/AgCl/saturated KCl as the reference electrode (RE, 0.197 V *vs.* SHE), attached to an Ivium CompactStat potentiostat/galvanostat/zero resistance ammeter. All glassware was cleaned with aqua regia and rinsed with water to avoid cross contamination. If not mentioned otherwise, the scan speed was set at 5 mV s^{-1} between 1.0 V and 1.5 V (*vs.* Ag/AgCl) to avoid bubble formation. The potential of the RE was measured with respect to a reversible hydrogen electrode (RHE) with Pt as the WE and CE. Prior to calibration, hydrogen was bubbled through the same electrolyte which was later used in the electrochemical characterization experiment for at least 15 min. All data presented are scaled to the RHE.

For the OER measurements, the system was saturated with O_2 for at least 15 min prior to the characterization of the WE. Ohmic drop correction was performed using electrochemical impedance spectroscopy (EIS) as well as the current interrupt method. All data were corrected for internal resistance (iR) using the Ivium Potentiostat software. To identify the region of interest, initial cyclovoltametric (CV) measurements were performed over a range of −0.1 to 1.6 V and the tested electrodes were discarded. The long term stability was tested by chronopotentiometry at 1 mA cm^{-2} over 7 h and at 10 mA cm^{-2} over 14 h.

4.2.2 Additional analytical techniques. AFM was performed on an MFP-3D AFM (Asylum Research/Oxford Instruments) in the intermittent contact mode with an Olympus cantilever (resonance frequency approximately 300 kHz). The height of one layer was determined over 30 edges. To exclude aberrations by chemical contrast between the substrate and IrOOH nanosheet, the height was determined on folded and/or overlapping nanosheets. The TEM samples were prepared by dropping the colloidal nanosheet suspension of the IrOOH nanosheets onto a lacey carbon film/copper grid (Plano) and subsequent drying under IR-light irradiation. TEM was performed with a Philips CM30 ST (300 kV, LaB_6 cathode), and with a CMOS camera (TemCam-F216, Tietz) for recording bright field images and SAED patterns. The simulation of the diffraction pattern was performed with the program JEMS (Stadelmann). PXRD was performed on a Stoe StadiP utilizing Ag-$K_{\alpha 1}$ radiation (Ge(111) monochromator, $\lambda = 0.559410$ Å) with a MythenK detector in Debye–Scherrer geometry. The program WinXPOW (Stoe) was used to analyze the PXRD data and LeBail fits were performed with the TOPAS program (Bruker AXS). X-ray photoelectron spectroscopy was carried out in a commercial Kratos Axis Ultra system with a monochromatized Al K_α source (1486.6 eV) with a base pressure in the lower 10^{-10} mbar range. The binding energy (BE) was calibrated by setting the C 1s BE to 284.8 eV with respect to the Fermi level. High-resolution spectra were acquired with an analyzer pass energy of 20 eV. Analysis of the XPS data was performed with CasaXPS software. The energy separation of the Ir $4f_{7/2}$ and Ir $4f_{5/2}$ was constrained to 2.98 eV.[50] The zeta potential was measured on the Zetasizer (Malvern). SEM imaging was performed on a Merlin SEM (Carl Zeiss AG).

Conflicts of interest

There are no conflicts to declare.

Acknowledgements

We gratefully acknowledge the financial support by the Max Planck Society, the German Science Foundation (DFG), the Nanosystems Initiative Munich (NIM), and the Center for Nanoscience (CeNS). Open Access funding provided by the Max Planck Society.

References

1 N. S. Lewis and D. G. Nocera, *Proc. Natl. Acad. Sci. U. S. A.*, 2006, **103**, 15729–15735.
2 J. Rossmeisl, Z.-W. Qu, H. Zhu, G.-J. Kroes and J. Nørskov, *J. Electroanal. Chem.*, 2007, **607**, 83–89.
3 M. T. Koper, *J. Electroanal. Chem.*, 2011, **660**, 254–260.
4 H. B. Gray, *Nat. Chem.*, 2009, **1**, 7.
5 N.-T. Suen, S.-F. Hung, Q. Quan, N. Zhang, Y.-J. Xu and H. M. Chen, *Chem. Soc. Rev.*, 2017, **46**, 337–365.
6 J. Bockris and T. Otagawa, *J. Electrochem. Soc.*, 1984, **131**, 290–302.
7 Y. Matsumoto and E. Sato, *Mater. Chem. Phys.*, 1986, **14**, 397–426.
8 Z. Lu, W. Xu, W. Zhu, Q. Yang, X. Lei, J. Liu, Y. Li, X. Sun and X. Duan, *Chem. Commun.*, 2014, **50**, 6479.
9 F. Song and X. Hu, *Nat. Commun.*, 2014, **5**, 4477.
10 M. G. Walter, E. L. Warren, J. R. McKone, S. W. Boettcher, Q. Mi, E. A. Santori and N. S. Lewis, *Chem. Rev.*, 2010, **110**, 6446–6473.
11 C. C. L. McCrory, S. Jung, J. C. Peters and T. F. Jaramillo, *J. Am. Chem. Soc.*, 2013, **135**, 16977–16987.
12 Y. Lee, J. Suntivich, K. J. May, E. E. Perry and Y. Shao-Horn, *J. Phys. Chem. Lett.*, 2012, **3**, 399–404.
13 G. Li, H. Yu, W. Song, X. Wang, Y. Li, Z. Shao and B. Yi, *Int. J. Hydrogen Energy*, 2012, **37**, 16786–16794.
14 S. Cherevko, S. Geiger, O. Kasian, N. Kulyk, J.-P. Grote, A. Savan, B. R. Shrestha, S. Merzlikin, B. Breitbach, A. Ludwig, *et al.*, *Catal. Today*, 2016, **262**, 170–180.
15 E. Ortel, T. Reier, P. Strasser and R. Kraehnert, *Chem. Mater.*, 2011, **23**, 3201–3209.
16 M. Hüppauff and B. Lengeler, *J. Electrochem. Soc.*, 1993, **140**, 598–602.
17 T. Reier, D. Teschner, T. Lunkenbein, A. Bergmann, S. Selve, R. Kraehnert, R. Schlögl and P. Strasser, *J. Electrochem. Soc.*, 2014, **161**, F876–F882.
18 M. Bernicke, E. Ortel, T. Reier, A. Bergmann, J. Ferreira de Araujo, P. Strasser and R. Kraehnert, *ChemSusChem*, 2015, **8**, 1908–1915.
19 V. Pfeifer, T. E. Jones, J. J. Velasco Vélez, C. Massué, R. Arrigo, D. Teschner, F. Girgsdies, M. Scherzer, M. T. Greiner, J. Allan, M. Hashagen, G. Weinberg, S. Piccinin, M. Hävecker, A. Knop-Gericke and R. Schlögl, *Surf. Interface Anal.*, 2016, **48**, 261–273.
20 D. Takimoto, K. Fukuda, S. Miyasaka, T. Ishida, Y. Ayato, D. Mochizuki, W. Shimizu and W. Sugimoto, *Electrocatalysis*, 2017, **8**, 144–150.
21 D. Takimoto, Y. Ayato, D. Mochizuki and W. Sugimoto, *Electrochemistry*, 2017, **85**, 779–783.
22 D. Weber, L. Schoop, D. Wurmbrand, J. Nuss, E. Seibel, F. F. Tafti, H. Ji, R. J. Cava, R. E. Dinnebier and B. V. Lotsch, *Chem. Mater.*, 2017, **29**, 8338–8345.
23 A. Lerf and R. Schoellhorn, *Inorg. Chem.*, 1977, **16**, 2950–2956.
24 D. Yang and R. Frindt, *J. Mater. Res.*, 1996, **11**, 1733–1738.
25 K. Szendrei, P. Ganter, O. Sànchez-Sobrado, R. Eger, A. Kuhn and B. V. Lotsch, *Adv. Mater.*, 2015, **27**, 6341–6348.
26 Y. Omomo, T. Sasaki, L. Wang and M. Watanabe, *J. Am. Chem. Soc.*, 2003, **125**, 3568–3575.
27 T. W. Kim, E.-J. Oh, A.-Y. Jee, S. T. Lim, D. H. Park, M. Lee, S.-H. Hyun, J.-H. Choy and S.-J. Hwang, *Chem.–Eur. J.*, 2009, **15**, 10752–10761.
28 W. Sugimoto, H. Iwata, Y. Yasunaga, Y. Murakami and Y. Takasu, *Angew. Chem., Int. Ed.*, 2003, **42**, 4092–4096.
29 T. Reier, Z. Pawolek, S. Cherevko, M. Bruns, T. Jones, D. Teschner, S. Selve, A. Bergmann, H. N. Nong, R. Schlögl, K. J. J. Mayrhofer and P. Strasser, *J. Am. Chem. Soc.*, 2015, **137**, 13031–13040.
30 F. Dionigi and P. Strasser, *Adv. Energy Mater.*, 2016, **6**, 1600621.

31 B. Zhang, X. Zheng, O. Voznyy, R. Comin, M. Bajdich, M. García-Melchor, L. Han, J. Xu, M. Liu, L. Zheng, F. P. García de Arquer, C. T. Dinh, F. Fan, M. Yuan, E. Yassitepe, N. Chen, T. Regier, P. Liu, Y. Li, P. De Luna, A. Janmohamed, H. L. Xin, H. Yang, A. Vojvodic and E. H. Sargent, *Science*, 2016, **352**, 333–337.
32 M. W. Kanan and D. G. Nocera, *Science*, 2008, **321**, 1072–1075.
33 C.-M. Chan and W. H. Weinberg, *J. Chem. Phys.*, 1979, **71**, 2788–2792.
34 W. Sun, Y. Song, X.-Q. Gong, L.-m. Cao and J. Yang, *ACS Appl. Mater. Interfaces*, 2016, **8**, 820–826.
35 C. Spöri, J. T. H. Kwan, A. Bonakdarpour, D. P. Wilkinson and P. Strasser, *Angew. Chem., Int. Ed.*, 2017, **56**, 5994–6021; *Angew. Chem.*, 2017, **129**, 6088–6117.
36 J.-M. Hu, J.-Q. Zhang and C.-N. Cao, *Int. J. Hydrogen Energy*, 2004, **29**, 791–797.
37 M. E. G. Lyons and S. Floquet, *Phys. Chem. Chem. Phys.*, 2011, **13**, 5314–5335.
38 J. M. Kahk, C. G. Poll, F. E. Oropeza, J. M. Ablett, D. Céolin, J.-P. Rueff, S. Agrestini, Y. Utsumi, K. D. Tsuei, Y. F. Liao, F. Borgatti, G. Panaccione, A. Regoutz, R. G. Egdell, B. J. Morgan, D. O. Scanlon and D. J. Payne, *Phys. Rev. Lett.*, 2014, **112**, 117601.
39 Z. Pavlovic, C. Ranjan, Q. Gao, M. van Gastel and R. Schlo̲g̲l, *ACS Catal.*, 2016, **6**, 8098–8105.
40 S. Cherevko, S. Geiger, O. Kasian, A. Mingers and K. J. Mayrhofer, *J. Electroanal. Chem.*, 2016, **774**, 102–110.
41 J. Kim, P.-C. Shih, K.-C. Tsao, Y.-T. Pan, X. Yin, C.-J. Sun and H. Yang, *J. Am. Chem. Soc.*, 2017, **139**, 12076–12083.
42 L. Trotochaud, J. K. Ranney, K. N. Williams and S. W. Boettcher, *J. Am. Chem. Soc.*, 2012, **134**, 17253–17261.
43 T. F. Jaramillo, K. P. Jørgensen, J. Bonde, J. H. Nielsen, S. Horch and I. Chorkendorff, *Science*, 2007, **317**, 100–102.
44 M. V. Bollinger, J. V. Lauritsen, K. W. Jacobsen, J. K. Nørskov, S. Helveg and F. Besenbacher, *Phys. Rev. Lett.*, 2001, **87**, 196803.
45 J. V. Lauritsen, J. Kibsgaard, S. Helveg, H. Topsøe, B. S. Clausen, E. Lægsgaard and F. Besenbacher, *Nat. Nanotechnol.*, 2007, **2**, 53.
46 O. Kasian, J.-P. Grote, S. Geiger, S. Cherevko and K. J. Mayrhofer, *Angew. Chem., Int. Ed.*, 2018, **57**, 2488–2491; *Angew. Chem.*, 2018, **130**, 2514–2517.
47 D. K. Bediako, A. M. Ullman and D. G. Nocera, *Catalytic oxygen evolution by cobalt oxido thin films*, Springer, 2015, pp. 173–213.
48 J. Li, R. Güttinger, R. Moré, F. Song, W. Wan and G. Patzke, *Chem. Soc. Rev.*, 2017, **46**, 6124–6147.
49 M. B. Stevens, L. J. Enman, A. S. Batchellor, M. R. Cosby, A. E. Vise, C. D. Trang and S. W. Boettcher, *Chem. Mater.*, 2016, **29**, 120–140.
50 J. Moulder, W. Stickle, P. Sobol, K. Bomben and J. Chastain, *Physical Electronics Division*, Perkin-Elmer, Eden Prairie, 1995, 1992.